Journal of
Materials Chemistry A

PAPER

View Article Online
View Journal | View Issue

Cite this: J. Mater. Chem. A, 2015, 3, 12786

Charge storage mechanism of activated manganese oxide composites for pseudocapacitors†

Tzu-Ho Wu,[a,c] David Hesp,[b] Vin Dhanak,[b] Christopher Collins,[a] Filipe Braga,[a] Laurence J. Hardwick*[a] and Chi-Chang Hu*[c]

Received 13th January 2015
Accepted 13th May 2015

DOI: 10.1039/c5ta03334a

www.rsc.org/MaterialsA

Manganese oxides can undergo an electrochemical activation step that leads to greater capacitances, of which the structural change and mechanism remains poorly understood. Herein we present a wide-ranging study on a manganese oxide synthesised by annealing manganese(II) acetate precursor to 300 °C, which includes *in operando* monitoring of the structural evolution during the activation process *via in situ* Raman microscopy. Based on powder X-ray diffraction, X-ray photoelectron spectroscopy, transmission electron and *ex situ* Raman microscopy, the as prepared manganese oxide was characterised as hausmannite-Mn_3O_4 with a minor portion of MnO_2. The activation process of converting as-prepared hausmannite-Mn_3O_4 into amorphous MnO_2 (with localised birnessite structure) by electrochemical cycling in 0.5 M Na_2SO_4 was examined. After activation, the activated MnO_x exhibited capacitive performance of 174 F g^{-1} at a mass loading of 0.71 mg cm^{-2}. The charge storage mechanism is proposed as the redox reaction between Mn(III) and Mn(IV) at outer surface active sites, since the disordered birnessite-MnO_2 does not provide an ordered layer structure for cations and/or protons to intercalate.

Introduction

Electrochemical supercapacitors have been widely investigated due to their high charge/discharge efficiency, high-rate charge storage and delivery, as well as long cycle life.[1] Recently, researchers have investigated approaches to increase the specific energy stored in supercapacitors in order to apply to numerous energy storage applications, such as hybrid electric vehicles, starting assistance to fuel cells, and power sources of electronics and cordless electric tools.[1–3] According to the charge storage mechanism, the non-faradaic electrical double-layer capacitors (EDLCs) are based on charge separation (*i.e.*, arrangement of ions/polar molecules) at the electrode/solution interface. The pseudocapacitance originates from the Faradaic redox reactions of electroactive species within electrode materials.

The capacitive performance of MnO_2 in neutral aqueous electrolytes has received much attention, due to improving cycle life (at least 10 000 cycles[4–6]), acceptable specific capacitance at moderate scan rates for MnO_2 thin films (100–400 F g^{-1}),[7–10] and low cost.[10–13] MnO_2 exhibits more than 0.9 V potential window in neutral media, such as alkali metal chloride,[10,14] alkali metal sulphate,[5,12] and specific lithium salts[15] aqueous electrolytes, without considering the significant enlargement of the cell voltage *via* the asymmetric design.[16–18] The charge storage mechanism of MnO_2 has been discussed by various analyses, such as X-ray photoelectron spectroscopy (XPS),[13] electrochemical quartz crystal microbalance (EQCM),[19] and *in situ* powder X-ray diffraction (PXRD).[14] Two mechanisms have been proposed to elucidate the MnO_2 charge storage process. The first is based on the surface adsorption of cations on MnO_2 active sites,[10] while the second involves the intercalation and expulsion of alkali metal cations and/or protons into/from MnO_2 structures.[20] The synergistic effect of MnO_2 and Mn_3O_4 has been proposed from our previous work,[21] which demonstrated that the specific current responses for MnO_2/Mn_3O_4 composites are superior than individual manganese oxides (MnO_x), *i.e.*, MnO_2 or Mn_3O_4 measured on single-crystalline MnOOH nanowires. Alternatively, the activation from hausmannite-Mn_3O_4 to birnessite-MnO_2 by electrochemical methods has been proposed by a series of PXRD, X-ray absorption spectroscopic (XAS), and *ex situ* Raman spectroscopic analyses.[22–26] The activation process has been

---

[a] Department of Chemistry, The University of Liverpool, Crown Street, Liverpool, L69 7ZD, UK. E-mail: laurence.hardwick@liv.ac.uk

[b] Department of Physics, The University of Liverpool, Crown Street, Liverpool, L69 7ZD, UK

[c] Department of Chemical Engineering, National Tsing Hua University, Hsin-Chu, 30013 Taiwan. E-mail: cchu@che.nthu.edu.tw

† Electronic supplementary information (ESI) available: Literature comparison, potential of quasi reference electrode measurement, Lorentz fitting of *ex situ* Raman spectra, XPS data and PXRD pattern of MnO_x after activation. See DOI: 10.1039/c5ta03334a

proposed as a complex and irreversible process, and the new formed birnessite-MnO_2 is accepted as the material responsible for pseudocapacitive behaviour *via* the insertion of cations and/or protons.[22,26] The structural disorder of electrochemically activated birnessite-MnO_2 has been previously remarked upon.[23] However, the charge storage mechanism of electrochemically activated birnessite-MnO_2 from hausmannite-Mn_3O_4 in neutral aqueous electrolytes has not yet been verified.

Raman spectroscopy is a powerful technique for the characterisation of short-range order of surface molecular species (especially for covalent character of the metal–oxygen bond).[27,28] Therefore, Raman analyses have been widely used to characterise various manganese oxides, since they possess a variety of oxidation states and phases.[28–33] The use of *in situ* measurement techniques are important in understanding the Mn_3O_4 activation process and charge storage mechanism in neutral aqueous electrolytes since the dried electrodes used in *ex situ* techniques may not represent the true state during electrochemical analyses.

A number of previous works have characterised the conversion of various manganese oxides into birnessite-MnO_2,[22–26,34] with applicable studies relating to electrochemical activation from Mn_3O_4 to MnO_2 that are detailed in Table S1.† Among these reported works, the as-prepared and electrochemically activated MnO_x were characterised as pure Mn_3O_4 and MnO_2 according to various *ex situ* analyses methods, respectively.[22–25] In the majority of studies, the MnO_x were identified as crystallised hausmannite-Mn_3O_4 and birnessite-MnO_2.[22,24,25] Consequently, the crystallinity of activated MnO_x is presumed to be dependent on the crystallinity of as-prepared Mn_3O_4. For example, the applied high temperature thermal reduction of electrolytic manganese dioxide at 1050 °C for 72 h is believed to be a well crystallised Mn_3O_4, which probably results in the highly crystallised birnessite structure after electrochemical activation.

In this study, the electrochemical activation of hausmannite-Mn_3O_4 in 0.5 M Na_2SO_4 was characterised by both *in situ* and *ex situ* techniques in order to understand both the activation process and the charge storage mechanism of this promising manganese oxide composite pseudo-capacitive material.

Experimental

The preparation of MnO_x material followed our previous work.[17] In short, the manganese(II) acetate tetrahydrate (99.99%, from Sigma-Aldrich) precursor solution annealed at a ramping rate of 1 °C min^{-1} to 300 °C and then left to cool down to ambient temperature. PXRD was measured using either a Cu K_α source ($\lambda = 1.54$ Å, Mac Science, MXP 18) for as-prepared MnO_x or a Mo K_α source ($\lambda = 0.709$ Å, Bruker, D8 advance) for activated MnO_x in Debye–Scherrer geometry with a capillary diameter of 0.5 mm. TEM analyses were conducted on a Philips Tecnai F20 G2 electron microscope at 200 kV, and samples for TEM analyses were prepared by drop casting on copper grids followed by solvent evaporation in air at 80 °C. The surface morphologies of MnO_x were examined by SEM (JEOL, JSM-6610 at 20 kV). XPS measurements were performed in a standard ultrahigh vacuum surface science chamber (2×10^{-10} mbar) a PSP Vacuum Technology electron energy analyzer (angle integrating ± 10°) and a dual anode Mg K_α (1253.6 eV) X-ray source.

For *in situ* Raman cell configuration, the working electrode was free-standing sample film composed of as-prepared MnO_x (30%), ground carbon black (XC-72, Cabot Corporation, USA, 173 m^2 g^{-1}; 20%), and poly(vinylidenefluoride-hexafluoropropylene) co-polymeric binder (Kynar-flex, Arkema) powders (50%). The counter electrode was prepared by casting activated carbon (ACS-679 from China Steel Chemical Corporation, Taiwan, 1635 m^2 g^{-1}) onto an Al current collector, while activated carbon free-standing film composed of ACS-679 activated carbon (40%) and Kynar-flex powders (60%) was served as the quasi-reference electrode (QRE).[35] The three-electrode compartments were sealed in the *in situ* Raman cell with adequate amount of electrolyte (4–5 drops).[36] The mass based on Mn_3O_4 of working electrode and activated carbon of counter electrode were *ca.* 1 mg and 15 mg, respectively. Note that the potential of QRE were tested in a beaker cell, the cyclic voltammetric (CV) profile of MnO_2 between −0.1 and 1.1 V was extremely similar to the CV measured against an Ag/AgCl (ALS co. Ltd, Japan, 3 M NaCl, 0.209 V *versus* SHE at 25 °C) in the range between 0 and 1.2 V, indicating that the potential difference of QRE and Ag/AgCl is *ca.* 0.1 V (Fig. S1†). The electrolyte was 0.5 M Na_2SO_4 degassed with purified argon gas flow before the measurements. *In situ* Raman spectra were recorded with Raman microscope (Renishaw inVia), using a He–Ne laser (632.8 nm) focussed through an inverted microscope (Leica), *via* a 50× objective lens (Leica). *In situ* Raman spectra were measured at different potentials with an interval of 200 mV, starting from 0.1 V *vs.* QRE to 1.1 V (positive sweep, PS) and then back from 0.9 V to −0.1 V (negative sweep, NS). Therefore, 12 spectra were obtained from each *in situ* Raman cycle. For each spectrum, the working electrode was pre-polarised for 3 min and held the potential during the spectral acquisition with the range of 250–750 cm^{-1}. The formation of Mn_3O_4 triggered by an increase in lattice temperature due to local heating by laser has been widely reported.[28,29,33] In order to avoid this factor, the laser exposed to sample surface was controlled *via* the use of an appropriate filter to keep below a maximum power of 0.37 mW.

For *ex situ* Raman experiments, the working electrodes were prepared by casting the slurry composed of as-prepared MnO_x (70%), XC-72 (20%), and Kynar (10%) onto graphite electrodes. Total mass of each electrode is 0.71 mg, which is used for calculating specific capacitance. An Ag/AgCl and a Pt wire were used as reference and counter electrodes, respectively. The measurements under the three-electrode mode were performed in deaerated 0.5 M Na_2SO_4 in a sealed beaker cell at 25 °C. The cyclic voltammograms were measured at 25 mV s^{-1} between 0 and 1.2 V (*vs.* Ag/AgCl). The MnO_x-coated working electrodes were potential-cycled for 5, 10, 50, 100, 150, 200, and 500 cycles to elucidate the activation process. After CV cycling, the MnO_x-coated electrodes were gently washed by deionised-water and dried in 85 °C oven overnight.

Results and discussion

Chemical synthesised as-prepared MnO_x

The diffraction pattern of as-prepared MnO_x (Fig. 1) corresponds to the PXRD pattern of hausmannite-Mn_3O_4 from the database (JCPDS CARD 24-0734). Reflections at 18.0°, 28.9°, 32.4°, 36.1°, and 59.8° are recorded, which correspond to face (101), (112), (103), (211), and (224) of hausmannite-Mn_3O_4, respectively. The sub-particles of the MnO_x can be observed by TEM images (Fig. 2b and c). From TEM images, the particle size of as-prepared MnO_x is *ca.* 6–8 nm. The *d*-spacing of 0.499, 0.313, 0.281, 0.253, 0.208, 0.182, 0.157, and 0.146 nm can be found and calculated from the selected area electron diffraction (SAED) pattern of as-prepared MnO_x (Fig. 2a), which are consistent with the *d*-spacing of hausmannite-Mn_3O_4. Moreover, the lattice spacing of 0.50, 0.31, 0.28, and 0.25 nm can be identified from the TEM image (Fig. 2c), which correspond to face (101), (112), (103), and (211) of hausmannite-Mn_3O_4, respectively. The diffraction peaks and *d*-spacing of as-prepared MnO_x are compiled and compared to hausmannite-Mn_3O_4 (JCPDS CARD 24-0734) in Table 1, which verifies that the as-prepared MnO_x can be considered as consisting of hausmannite-Mn_3O_4.[13,37–39] The mean manganese oxidation state of MnO_x can be determined by the energy separation between the two peaks of Mn 3s core level spectrum.[13,37–39] It has been reported that more interaction can occur upon photoelectron ejection since a lower valence state implies more electrons in the 3d orbital. Consequently, the energy separation between the two components of the Mn 3s multiplet will increase.[13,38] The energy separation between these two peaks of Mn 3s spectra is 5.79, 5.50, 5.41, and 4.78 eV for reference sample of MnO, Mn_3O_4, Mn_2O_3, and MnO_2, respectively.[13,38,39] The peak separation is 5.23 eV obtained from Mn 3s spectrum of as-prepared MnO_x (Fig. 3a). Therefore, the mean manganese oxidation state of as-prepared MnO_x is *ca.* 3.18 according to the relationship of energy separation and mean oxidation state,[13,38,39] which implies that as-prepared MnO_x possesses a minor portion of Mn(IV) since the mean oxidation state of as-prepared MnO_x is slightly higher than Mn_3O_4 (mean oxidation state = 2.67). XPS is a surface-sensitive measurement, which indicates the mean manganese oxidation state obtained from XPS results is in the proximity to the sample surface. From Mn 2p spectrum of as-prepared MnO_x (not shown here), the peaks of Mn $2p_{3/2}$ and Mn $2p_{1/2}$ are located at 641.91 and 653.31 eV, respectively. From the Lorentz fitting of O 1s spectrum of as-prepared MnO_x (Fig. 3b), the peak position at 529.8, 531.3, and 532.5 eV are attributed to Mn–O–Mn (for anhydrous oxide), Mn–OH (hydroxide), and H–O–H bonds (crystalline water), respectively.[13,37–39] The Mn–OH bonds contribute 15% (Table 2), which suggests the as-prepared MnO_x exhibit better capacitive performance since the hydrous property facilitates ionic exchange.[37,39]

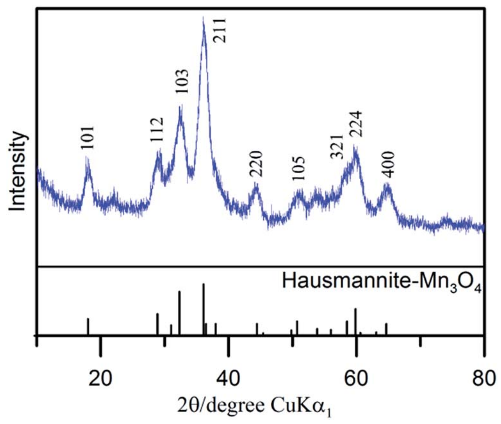

Fig. 1 X-ray diffraction pattern of as-prepared MnO_x.

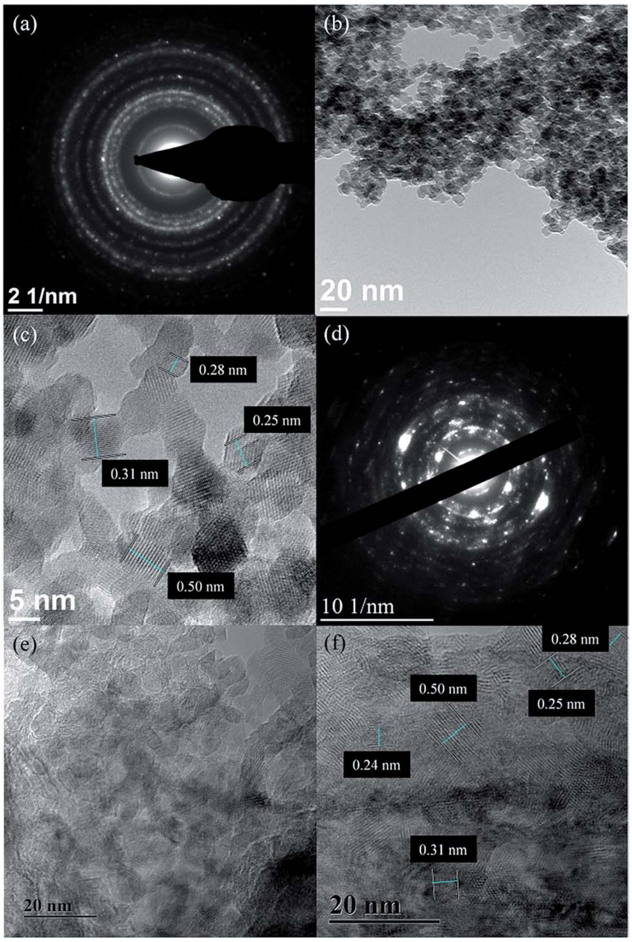

Fig. 2 (a and d) SAED pattern and (b, c, e and f) TEM images of (a–c) as-prepared and (d–f) activated MnO_x.

According to literature,[40] the Raman active bands of hausmannite-Mn_3O_4 are observed at 289, 315, 370, 477, and 660 cm^{-1}. Bands at 310–320 and 360–370 cm^{-1} are the bending mode of Mn_3O_4, while 650–660 cm^{-1} is the Mn–O breathing vibration of Mn^{2+} in tetrahedral coordination.[23,31] In general, the Raman active bands for MnO_2 are at 500–510, 575–585, and 625–650 cm^{-1}, which represent Mn–O stretching vibration of MnO_6 octahedra, Mn–O stretching vibration of the basal plane of MnO_6 sheets, and the symmetric stretching vibration of Mn–O of the MnO_6 group, respectively.[23,32] The Raman spectrum of as-prepared MnO_x is shown in Fig. 4. The intense peak

Table 1 Comparisons of diffraction peaks and *d*-spacing calculated from the SAED pattern of as-prepared and activated MnO_x with standards (hausmannite-Mn_3O_4, JCPDS CARD 24-0734 and birnessite-MnO_2, JCPDS CARD 18-0802) from database

	2θ from XRD pattern (degree)	2θ from database (degree)	*d*-spacing calculated from SAED pattern (nm)	*d*-spacing from Mn_3O_4 database (nm)		*d*-spacing calculated from SAED pattern (nm)	*d*-spacing from MnO_2 database (nm)
As-prepared MnO_x	18.0	18.0	0.499	0.492	Activated MnO_x	0.497	
	28.9	28.9	0.313	0.309		0.308	
		31.0		0.288			
	32.4	32.3	0.281	0.277		0.283	
	36.1	36.1	0.253	0.249		0.253	
						0.242	0.244
	44.3	44.4	0.208	0.204			
						0.210	0.212
		49.8	0.182	0.183		0.182	
	50.7	50.7		0.180			
	58.4	58.5	0.157	0.158		0.158	
	59.8	59.8		0.154			
	64.7	64.7	0.146	0.144		0.146	

at *ca.* 658 cm^{-1} can be observed, which is the most notable band of Mn_3O_4.[23,31] However, a shoulder around 575 cm^{-1} can also be found, which provides further evidence that as-prepared MnO_x might not be pure hausmannite-Mn_3O_4, since a minor portion of MnO_2 can be found in the spectrum. Moreover, the two peaks at 310–320 and 360–370 cm^{-1} are not able to be resolved from the background noise. The presence of (a minor portion) MnO_2 in the as-prepared MnO_x might reduce crystallinity of hausmannite-Mn_3O_4, which might result in the absence of the bending mode of Mn_3O_4. The results from both Raman and XPS analyses of as-prepared MnO_x strongly indicate a minor portion of Mn(IV) is present. According to the above analyses, the as-prepared MnO_x can be considered to be hausmannite-Mn_3O_4 with a minor portion of Mn(IV).

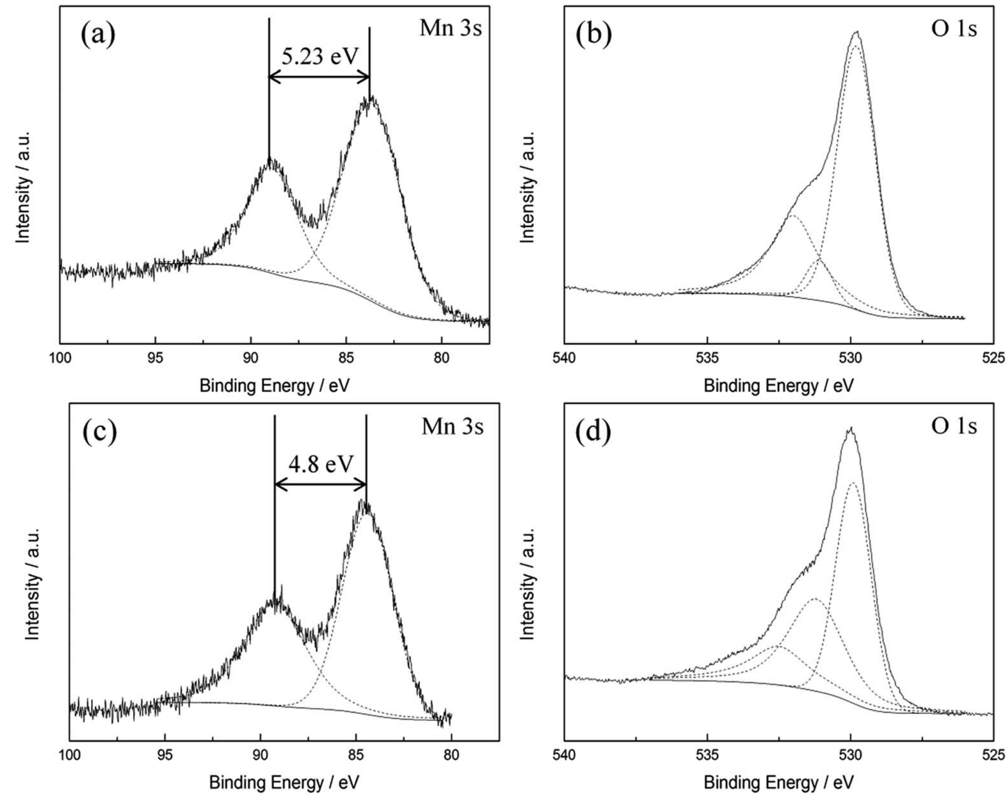

Fig. 3 XPS (a and c) Mn 3s, (b and d) O 1s spectra of (a and b) as-prepared and (c and d) activated MnO_x.

Table 2 Peak position and area percentage of O 1s spectrum of as-prepared and activated MnO_x

O 1 s		Position (eV)	Percentage (%)		Position (eV)	Percentage (%)
Mn–O–Mn	As-prepared MnO_x	529.8	67	Activated MnO_x	529.9	44
Mn–OH		531.3	15		531.2	37
H–O–H		532.5	18		532.5	19

Electrochemical activation process of MnO_x

CVs measured at a sweep rate of 25 mV s^{-1} between 0 and 1.2 V (*vs.* Ag/AgCl) in 0.5 M Na_2SO_4 for controlled cycles are shown in Fig. 5. For the first few cycles, the anodic peak around 1.05 V on the positive sweep can be considered to be the oxidation of Mn_3O_4 to higher oxidation state. This anodic peak gradually decreased during cycling, and the cathodic peak around 0.9 V on the negative sweep gradually decreased at the same time. On the other hand, the current responses of the redox peak at *ca.* 0.4–0.5 V gradually increased during cycling. This peak is related to partial oxidation/reduction between Mn(III) and Mn(IV) according to the Pourbaix diagram.[41] The rectangular CV profile at 500th cycle indicates that ideal capacitive performances of MnO_x can be obtained by potential cycling which has been proposed as an electrochemical activation method.[21] Note that the poor capacitive performance at first few cycles for pure Mn_3O_4 (*i.e.*, less than 20 F g^{-1}) has been reported.[22,24] However, the specific capacitance at 5th cycle reaches *ca.* 130 F g^{-1} in this work, which confirms that the as-prepared MnO_x is composed of a minor portion of MnO_2 and is not pure Mn_3O_4.

For the 1st *in situ* Raman cycle (Fig. 6a), a strong peak located at 658 cm^{-1} is visible from PS 0.1 V, PS 0.3 V, and PS 0.5 V. This peak is the characteristics of Mn_3O_4 as described above. From PS 0.9 V to NS −0.1 V, this peak slightly shifts to a lower wavenumber (from 658 to 650 cm^{-1}) with further applying potential. Besides, the intensity of this peak for the 12 spectra remains in the same level. On the other hand, a descending shoulder from *ca.* 650 to 550 cm^{-1} is found from PS 0.1 V. The peak at 575 cm^{-1} was gradually formed during the polarisations, and this peak became significant from PS 0.7 V to NS −0.1 V. Since the peak intensity of 575 cm^{-1} reached the same level of the peak at *ca.* 658 cm^{-1}, a new MnO_x species (*i.e.*, MnO_2) is believed to be formed. The spectra recorded at the 2nd cycle (Fig. 6b) all remain the similar pattern, which indicate that the newly formed MnO_2 remains stable in the cycled potential window. Therefore the mean Mn oxidation state during further cycling after activation can only be accessed *via* other techniques such as X-ray photoelectron spectroscopy or X-ray absorption microscopy.

Lorentz fitting of Raman spectra is used in order to gain a further understanding of this phenomenon. The peaks at 658, 477, and 289 cm^{-1} are related to hausmannite-Mn_3O_4,[40] while the peaks at 648, 618, 575, 506, and 408 cm^{-1} are attributed to birnessite-MnO_2.[33] Note that all the peak positions are fixed except for the peak at *ca.* 289 cm^{-1} (allows from 283 to 289 cm^{-1}). The Mn_3O_4 peak intensity at 658 cm^{-1} gradually decreased, while peaks related to birnessite-MnO_2 (marked as red line in Fig. 7) gradually enhanced during polarisations. The Mn_3O_4 peak at 658 cm^{-1} dominates for the 1st cycle PS 0.1 V and the 1st cycle PS 0.5 V. However, the peak at 648 cm^{-1} related to birnessite-MnO_2 became stronger than the Mn_3O_4 peak at 658 cm^{-1} with the positive and negative shifts in electrode potentials. As a result, this peak shifted from 658 (1st cycle PS 0.9 V) to 650 cm^{-1} (1st cycle NS −0.1 V) and further remained the same position. The peak intensity ratio of MnO_2 and Mn_3O_4 ($I_{MnO_2}/I_{Mn_3O_4}$) is proposed to be an indicator to quantify the degree of activation from Mn_3O_4 to MnO_2 although the different MnO_x species show different Raman sensitivities. Here, $I_{MnO_2}/I_{Mn_3O_4}$ is calculated on the basis of the peak intensity of 575 and 658 cm^{-1} from the fitting results since these two peaks are the

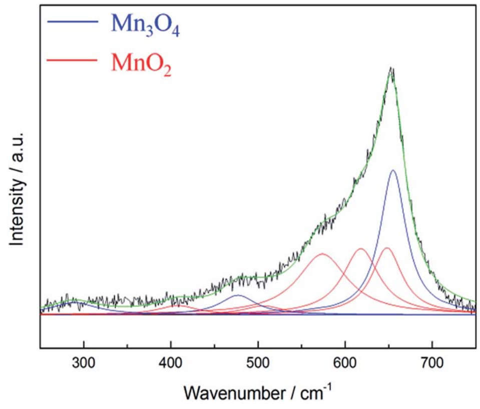

Fig. 4 Lorentz fitting of *ex situ* Raman spectrum of as-prepared MnO_x. Green line = envelope of total of the fitted peaks.

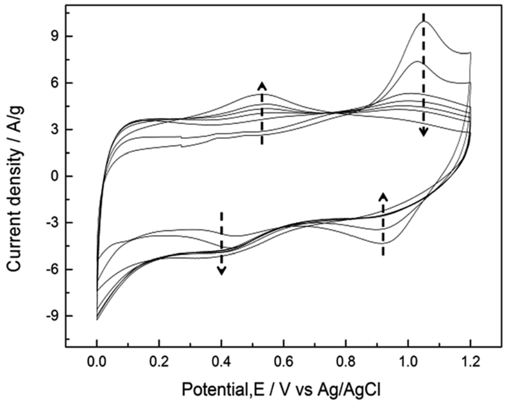

Fig. 5 CVs measured at a sweep rate of 25 mV s^{-1} between 0 and 1.2 V (*vs.* Ag/AgCl) in 0.5 M Na_2SO_4 for 5, 10, 50, 100, 150, 200, and 500 cycles.

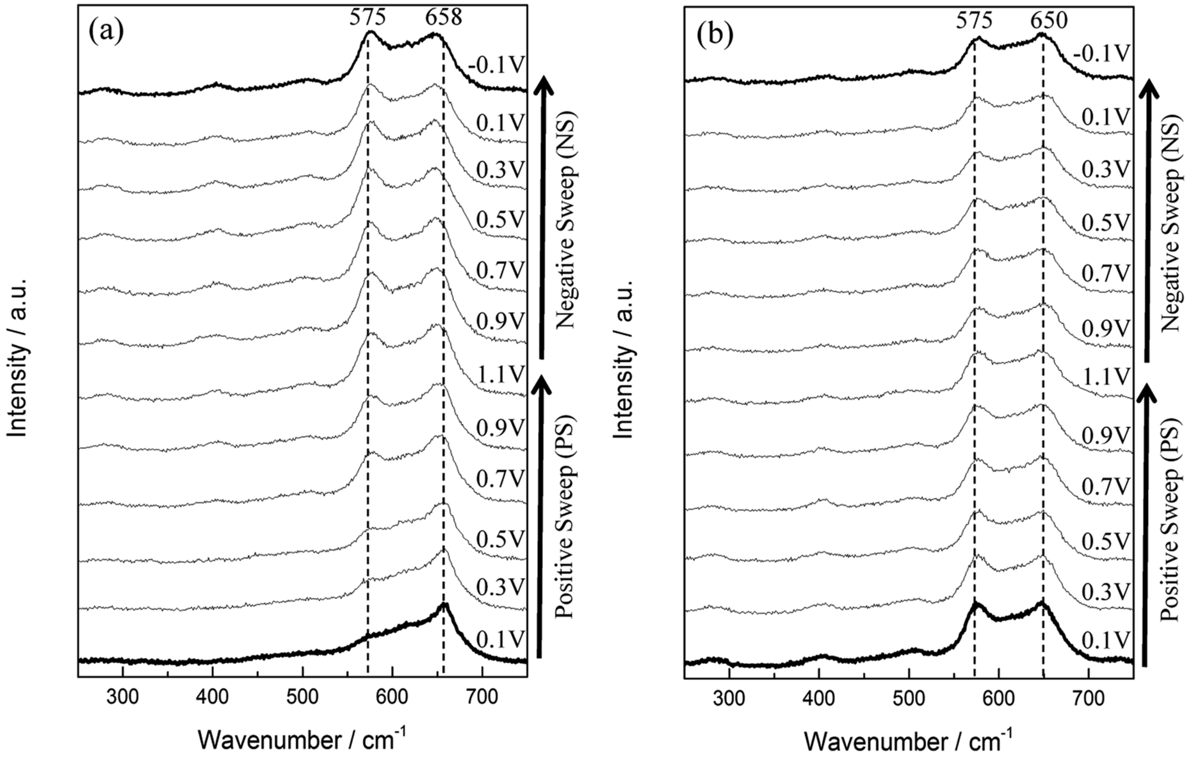

Fig. 6 *In situ* Raman spectra series of (a) the 1st and (b) the 2nd cycle of MnO_x. Each cycle started from 0.1 V (PS 0.1 V) and ended at −0.1 V (NS −0.1 V).

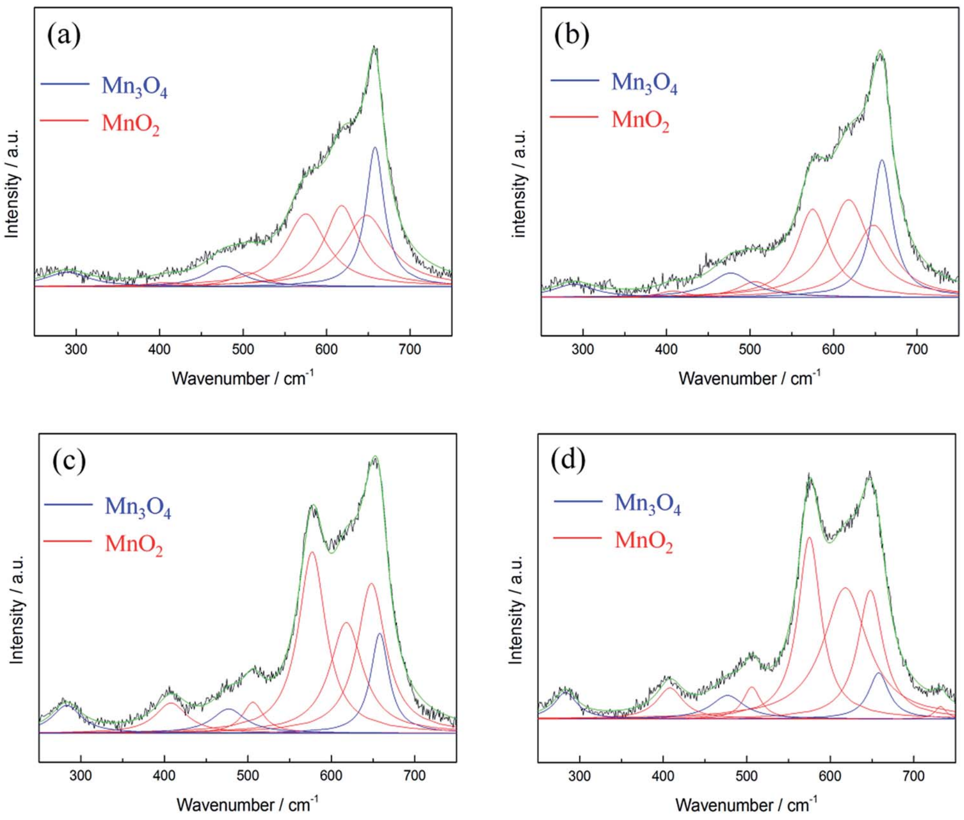

Fig. 7 Lorentz fitting of *in situ* Raman spectra of MnO_x (a) 1st cycle PS 0.1 V, (b) 1st cycle PS 0.5 V, (c) 1st cycle PS 0.9 V, and (d) 2nd cycle PS 0.1 V. Green line = envelope of total of the fitted peaks.

best representatives (the most distinguished peaks) for MnO_2 and Mn_3O_4, respectively. $I_{MnO_2}/I_{Mn_3O_4}$ for as-prepared MnO_x is 0.42 (Table S2†), and the value increases gradually during the electrochemical polarisations. $I_{MnO_2}/I_{Mn_3O_4}$ is 3.94 for the 2nd cycle PS 0.1 V, which is *ca.* 8 times higher than as-prepared MnO_x (Table 3). The mean manganese oxidation state of activated MnO_x is *ca.* 3.94 based on the energy separation (4.85 eV) of Mn 3s core level spectrum (Fig. 3c). Comparing with the mean manganese oxidation state of as-prepared MnO_x (3.18), the results support the activation from Mn_3O_4 (*i.e.*, Mn(II) and Mn(III)) to MnO_2 (Mn(IV)) during the electrochemical activation.

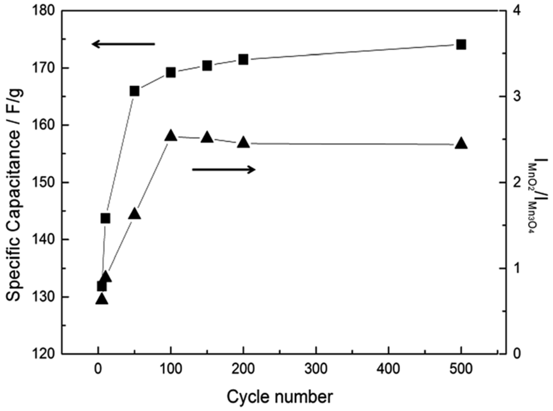

Fig. 8 Cycle number dependence of specific capacitance calculated by CV at 25 mV s^{-1} and intensity ratio (I_{MnO_2} of 575 cm^{-1}/$I_{Mn_3O_4}$ of 658 cm^{-1}) of MnO_x.

According to the fitting results, residual Mn_3O_4 can be still observed even at the 2nd *in situ* Raman cycle (Fig. 7d). Note that the formed MnO_2 is stable in the cycled potential window for the 2nd *in situ* Raman cycle (Fig. 6b). It therefore be concluded that not all the Mn_3O_4 is converted to MnO_2 in the above electrochemical treatment. Due to the residual Mn_3O_4, the mean manganese oxidation state for the activated MnO_x is not exactly equal to 4.0. Hence, it can be concluded that the major portion of hausmannite-Mn_3O_4 can be activated to birnessite-MnO_2 by the electrochemical treatment. Besides, the residual Mn_3O_4 in electrochemically activated birnessite-MnO_2 results in structure disorder of layered birnessite-MnO_2, which reasonably explains why the oxide derived from Mn_3O_4 showed higher cycling stability because of the coexistence of MnO_2 and Mn_3O_4.[21] *Ex situ* Raman spectra were recorded for all CV-cycled MnO_x. From Lorentz fitting results, the correlation between specific capacitance of MnO_x and CV cycle number is shown in Fig. 8. Note that the current responses related to the activation from Mn_3O_4 to MnO_2 (the anodic peak around 1.05 V on the positive sweep) are evident in the first few cycles, which decreases gradually during the activation process. The ideal pseudocapacitance of MnO_2 mainly contributes from the potential window between 0.2 and 0.8 V.[19] The current responses related to the oxidation of Mn_3O_4 cannot be considered pseudocapacitance. Therefore, the calculation in Fig. 8 is based on the baseline of 500th cycle (stable current responses) between 0.8 and 1.2 V. In general, MnO_2 is electrochemically active and reversible for supercapacitor applications[10] comparing with Mn_3O_4, which is known as a relatively electrochemical irreversible material among MnO_x species. The specific capacitance of MnO_x rapidly increased within the initial 50 cycles, which suggests that the activation from Mn_3O_4 to MnO_2 is relatively fast. With further cycling, the specific capacitance of MnO_x gradually increased and reached the stable level (*ca.* 170 F g^{-1}) from the 150th to the 500th cycle. Based on the Lorentz fitting of *ex situ* Raman spectra (Fig. S2†), the rapid increase of MnO_2 content ($I_{MnO_2}/I_{Mn_3O_4} = 0.63$ and 2.53 for 5th and 100th cycle, respectively) shows the same trend as capacitance increase. With further cycling to 500th cycle, $I_{MnO_2}/I_{Mn_3O_4}$ remained the same level (*i.e.*, 2.45). It should be noted that this ratio is lower than that from *in situ* measurements (3.94). Accordingly, the activation from hausmannite-Mn_3O_4 to birnessite-MnO_2 can be verified by the *in situ* and *ex situ* Raman experiments. The stable electrochemically activated birnessite-MnO_2 can be formed and displays promising pseudocapacitance in 0.5 M Na_2SO_4.

Fig. 9 shows the surface morphology change MnO_x during electrochemical activation. A compact surface morphology of as-prepared MnO_x can be observed in Fig. 9a, while it gradually changes into a porous surface after electrochemical activation (Fig. 9b–d). It has been proposed that the porous surface layer is the re-deposition of dissolved Mn(II) (from hausmannite-Mn_3O_4 crystalline structure) onto the electrode surface as MnO_2 during the activation process *via* CV cycling.[25] The proposed mechanism is reasonable since MnO_2 can be successfully formed from Mn(II) precursor by potentiodynamic method.[12] Besides, the insignificant electrochemical activation of Mn_2O_3 comparing with Mn_3O_4 has been found.[25] Therefore, dissolution of Mn(II) from MnO_x crystalline is believed to be the key for the electrochemical activation process. In fact, from the investigation of amorphous MnO_2 by electrochemical quartz crystal microbalance (EQCM), the porous surface of MnO_x (predominate MnO_2) is not only from the re-deposition of dissolved Mn(II) during electrochemical activation process but also from the re-deposition (at *ca.* 0.8–0.2 V) of dissolved Mn(IV) (at *ca.* 0.8–1.0 V) during CV cycling.[19] The normalised area of C 1s and Mn 3s XPS spectra of as-prepared and activated MnO_x are listed in Table S3.† In comparison with as-prepared MnO_x, the normalised

Table 3 Peak position (cm^{-1}) and full width at half maximum (FWHM, cm^{-1} in parenthesis) of the Mn_3O_4 and MnO_2 peaks by Lorentz fitting

	Mn_3O_4	MnO_2	MnO_2	MnO_2	MnO_2	Mn_3O_4	MnO_2	Mn_3O_4	$I_{MnO_2}/I_{Mn_3O_4}$
1st cycle PS 0.1 V	658 (27)	648 (66)	618 (51)	575 (61)	506 (45)	477 (55)	408 (55)	289 (65)	0.52
1st cycle PS 0.5 V	658 (29)	648 (58)	618 (60)	575 (47)	506 (50)	477 (60)	408 (40)	284 (61)	0.65
1st cycle PS 0.9 V	658 (26)	648 (42)	618 (48)	575 (40)	506 (31)	477 (48)	408 (46)	283 (43)	1.81
2nd cycle PS 0.1 V	658 (29)	648 (37)	618 (64)	575 (33)	506 (26)	477 (48)	408 (38)	283 (33)	3.94

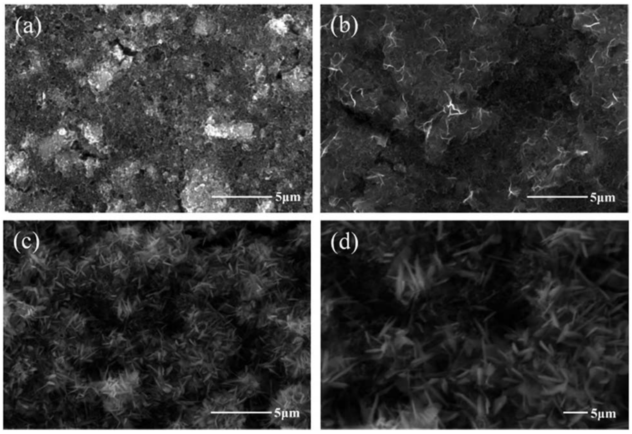

Fig. 9 SEM images of (a) as-prepared MnO_x and after (b) 100 (c and d) after 500 CV cycles in 0.5 M Na_2SO_4.

area ratio (C 1s/Mn 3s) of activated MnO_x reduced from *ca.* 2.59 to 1.04, indicating the re-deposition of MnO_2 onto the electrode surface suppressing the intensity of carbon black and polymeric binder.[25] Note that the intensity (counts/second) of XPS spectra strongly depends on the distance between samples and X-ray beam source. Therefore, normalised area (by atomic sensitivity factor) instead of absolute intensity is used in this work. Moreover, from SEM images (Fig. 9d), the porous nanostructure surface forms at the outer surface, while this structure cannot be found in some deeper regions. This suggests the electrochemical activation starts from outermost layer of Mn_3O_4 surface and then gradually into the bulk. This finding is consistent with literature, which reported the amorphous and hydrous MnO_2 is formed in the outer electrode layers and proceeds to grow at the expense of the remaining bulk crystalline Mn_3O_4.[42]

Electrochemically activated MnO_x and its charge–discharge mechanism

The activated MnO_x was characterised by PXRD as amorphous MnO_2 (Fig. S3†). The SAED pattern of activated MnO_x (Fig. 2d) suggests that the electrochemically activated MnO_x within the electrode composite possess poor crystallised structure since the diffraction patterns do not have well defined rings.

Interestingly, with further analysis, both birnessite-MnO_2 and hausmannite-Mn_3O_4 crystallites can be found in the activated MnO_x (Table 1) although no reflections can be observed from diffraction pattern of activated MnO_x. The *d*-spacing of 0.242 and 0.210 nm are corresponding to birnessite-MnO_2. Apart from these two *d*-spacing found in SAED pattern, others are all related to Mn_3O_4 residual in the activated MnO_x. From the TEM images of activated MnO_x (Fig. 2e), the particle-like MnO_x structure can be still observed. Compare to as-prepared MnO_x, the particles and lattices of activated MnO_x are not well defined. As a result, the activated MnO_x is believed to have disordered layered birnessite structure; however, there is insufficient long-range order to allow for a PXRD pattern to be observed. Therefore, the structure of the electrochemically activated MnO_x is determined to be composite material consisting of amorphous MnO_2 (with localised birnessite structure) and a minor portion of residual of hausmannite-Mn_3O_4. Amorphous manganese oxide has been considered to be beneficial for supercapacitors since it provides large interlayer distance and surface area-to-volume ratio. The increase contact between the electrolyte and the electrode material improves the utilisation ratio of the material.[43] Besides, the significant increase of Mn–OH (hydroxide) bond in activated MnO_x (Fig. 3d and Table 2) indicates that the MnO_x became more hydrous after electrochemical activation. As discussed above, hydrous property of MnO_x facilitates ionic exchange and exhibits better capacitive performance.[37,39]

The structure transformation from hexagonal to monoclinic due to cation (Na^+) intercalation into birnessite-MnO_2 has been reported,[44] as well as the subtle change of Raman spectra of birnessite-MnO_2 with and without cation (Li^+ and Na^+) intercalated in MnO_2 bilayers.[32] The intercalation of alkali-ion into birnessite-MnO_2 bilayers causes local lattice distortion, which results in shorter Mn–O chemical bonds (decrease of the interlayer spacing) and partial reduction of Mn^{4+} ions. As a result, the Mn–O symmetric stretching mode moves toward low wavenumber side upon alkali-ion intercalation.[32] However, this peak shift phenomenon due to cation intercalation into layers of birnessite-MnO_2 was not observed by *in situ* Raman during activation process in this work. Moreover, the peak positions of MnO_2 correspond to birnessite-MnO_2 rather than Na–birnessite-MnO_2 from literature.[32,33] Moreover, the peak around 732 cm^{-1}, identified as a vibrational mode for non-cation intercalated birnessite-MnO_2, can be observed by the Raman spectrum of activated MnO_x (Fig. 7d). This indicates that electrochemically activated birnessite structure might not possess a well-defined layer structure (*i.e.*, structure disordering) to allow cation (Na^+) intercalation into bilayers.

The XPS Na 1s spectrum of as-prepared MnO_x, activated MnO_x and a sodium intercalated MnO_2 sample ($Na_{0.33}MnO_2$) are shown in Fig. S4.† The Na 1s peak was present at 1072.2 eV (FWHM = 1.85) for activated MnO_x and shows *ca.* 1 eV shift in comparison to $Na_{0.33}MnO_2$ at 1071.2 eV (FWHM = 1.77). The binding energy at 1072–1073 eV is related to the Na–F bonding, which is attributed to the Na^+ (from Na_2SO_4 electrolyte) bonding with co-polymeric binder at F sites.[45] Although the Na/Mn ratio of activated MnO_x (1.03) is higher than $Na_{0.33}MnO_2$ (Na/Mn = 0.52), the Na element contributes from the Na–F bonding rather than incorporation into the MnO_x structure after electrochemical measurements.

Based upon the *in situ* Raman and Na 1s XPS analyses, cations are believed to reach the outer surface active sites of electrochemically activated birnessite-MnO_2 and the capacitive behaviour is attributable to the redox reaction between Mn(III) and Mn(IV). The relatively high specific surface area of as-prepared MnO_x (241 $m^2\ g^{-1}$) can provide abundant outer surface active sites. As a result, high specific capacitance of birnessite-MnO_2 can be obtained (*i.e.*, the specific capacitance measured at 500th is 174 F g^{-1}) by potential cycling, which can be compared with values of similar materials in the literature (Table S4†).[22–25] The capacitance normalised to specific surface area (C_{SA}) is *ca.* 72.3 μF cm^{-2}, which is higher than the double layer capacitance (*ca.* 10–20 μF cm^{-2}) for high surface area (over 1000 m^2 g^{-1}) carbon material.[1] The real C_{SA} of electrochemically activated birnessite-MnO_2 should be even higher since the calculation is based on the specific surface area of as-prepared MnO_x and the material might lose some part of active surface area during electrode preparation. Based on the calculated high C_{SA}, the charge storage of electrochemically activated MnO_x is attributed to the redox reaction between Mn(III) and Mn(IV) (pseudocapacitance).

The one-pot synthesised as-prepared MnO_x is characterised as hausmannite-Mn_3O_4 with a minor portion of MnO_2. The electrochemically activated MnO_x is characterised as a composite material consisting of localised birnessite structure MnO_2 and a minor portion of hausmannite-Mn_3O_4. The improved capacitive performance of activated MnO_x is attributed to the synergistic effect of poorly crystallised MnO_2 and Mn_3O_4 in the composite material, and this work describes routes of generating composite materials that possess greater electrochemical performance.

Conclusions

Electrochemically activated MnO_x, from one-pot synthesised hausmannite-Mn_3O_4, exhibits a capacitive performance of 174 F g^{-1} (at 25 mV s^{-1}) and 1.2 V potential window (0–1.2 V *vs.* Ag/AgCl), which is superior to reported values of comparable materials. Activation from primarily hausmannite-Mn_3O_4 to predominantly localised birnessite-MnO_2 by potential cycling is verified by both *in situ* and *ex situ* Raman microscopy, XPS and TEM analysis. Due to the structural disordering of electrochemically activated birnessite-MnO_2 and residual Mn_3O_4, the charge storage is attributable to the redox reaction between Mn(III) and Mn(IV) at outer surface active sites, rather than cations and/or protons intercalation into layer structures. The improved capacitive performance relates to the synergistic effect of well-dispersed MnO_2 and Mn_3O_4 nanoscale domains present within the activated material. Overall we show that the integrated nanoscale structuring of different phases of manganese oxides offers superior properties compared to bulk parent materials, and as such offers an avenue of future supercapacitor materials development.

Acknowledgements

This research is funded by the National Science Council and Ministry of Science Technology of Taiwan under contract no. 101-2221-E-007-112-MY3, 102-2221-E-007-120-MY3, 103-2911-I-007-515, 103-3113-E-006-009, and also supported by the boost program of the Lower Carbon Energy Research centre in NTHU. The financial support of this work, by the Ministry of Science and Technology, Taiwan and The Royal Society, UK, is gratefully acknowledged, as well as the Science without Borders Program, Ministério da Educação, Coordenação de Aperfeiçoamento de Pessoal de Nível Superior (CAPES) Brazil; and the Engineering and Physical Sciences Research Council (EPRSC) under grant EP/H000925. We would like to thank Ming-Guan Chen (Department of Chemical Engineering, National Tsing Hua University, Taiwan). From the University of Liverpool UK, we acknowledge T. Whittles & M. Althobaiti (Stephenson Institute for Renewable Energy) for XPS measurements and Ming Liu (Department of Chemistry) for BET and Tobias Heil (Nano Investigation Centre at Liverpool) for TEM analyses. Part of the work was carried out within the cooperative framework set-up between National Tsing Hua University, Taiwan and University of Liverpool, UK.

Notes and references

1 R. Kötz and M. Carlen, *Electrochim. Acta*, 2000, **45**, 2483–2498.
2 P. Simon and Y. Gogotsi, *Nature Mater.*, 2008, **7**, 845–854.
3 J. M. Miller and A. F. Burke, *Electrochem. Soc. Interface*, 2008, **17**, 53–57.
4 L. Athouël, F. Moser, R. Dugas, O. Crosnier, D. Bélanger and T. Brousse, *J. Phys. Chem. C*, 2008, **112**, 7270–7277.
5 T. Brousse, P. L. Taberna, O. Crosnier, R. Dugas, P. Guillemet, Y. Scudeller, Y. Zhou, F. Favier, D. Bélanger and P. Simon, *J. Power Sources*, 2007, **173**, 633–641.
6 T. Brousse, M. Toupin and D. Bélanger, *J. Electrochem. Soc.*, 2004, **151**, A614.
7 C. C. Hu and T. W. Tsou, *Electrochem. Commun.*, 2002, **4**, 105–109.
8 M. Toupin, T. Brousse and D. Bélanger, *Chem. Mater.*, 2002, **14**, 3946–3952.
9 H. Xia, W. Xiao, M. O. Lai and L. Lu, *Nanoscale Res. Lett.*, 2009, **4**, 1035–1040.
10 H. Y. Lee and J. B. Goodenough, *J. Solid State Chem.*, 1999, **144**, 220–223.
11 S. W. Zhang and G. Z. Chen, *Energy Mater.*, 2008, **3**, 186–200.
12 C. C. Hu and C. C. Wang, *J. Electrochem. Soc.*, 2003, **150**, A1079.
13 M. Toupin, T. Brousse and D. Belanger, *Chem. Mater.*, 2004, **16**, 3184–3190.
14 N. L. Wu and S. L. Kuo, *J. Electrochem. Soc.*, 2006, **153**, A1317–A1324.
15 A. Boisset, L. Athouël, J. Jacquemin, P. Porion, T. Brousse and M. Anouti, *J. Phys. Chem. C*, 2013, **117**, 7408–7422.
16 C. L. Liu, K. H. Chang, C. C. Hu and W. C. Wen, *J. Power Sources*, 2012, **217**, 184–192.
17 T. H. Wu, Y. H. Chu, C. C. Hu and L. J. Hardwick, *Electrochem. Commun.*, 2013, **27**, 81–84.
18 V. Khomenko, E. Raymundo-Piñero and F. Béguin, *J. Power Sources*, 2006, **153**, 183–190.
19 Y. H. Chu, C. C. Hu and K. H. Chang, *Electrochim. Acta*, 2012, **61**, 124–131.
20 S. C. Pang, M. A. Anderson and T. W. Chapman, *J. Electrochem. Soc.*, 2000, **147**, 444.
21 C. C. Hu, C. Y. Hung, K. H. Chang and Y. L. Yang, *J. Power Sources*, 2011, **196**, 847–850.
22 Y. Dai, K. Wang and J. Xie, *Appl. Phys. Lett.*, 2007, **90**, 104102.
23 K. W. Nam and K. B. Kim, *J. Electrochem. Soc.*, 2006, **153**, A81.
24 D. P. Dubal, D. S. Dhawale, R. R. Salunkhe and C. D. Lokhande, *J. Alloys Compd.*, 2010, **496**, 370–375.

25 S. Komaba, T. Tsuchikawa, A. Ogata, N. Yabuuchi, D. Nakagawa and M. Tomita, *Electrochim. Acta*, 2012, **59**, 455–463.
26 C. C. Hu, Y. T. Wu and K. H. Chang, *Chem. Mater.*, 2008, **20**, 2890–2894.
27 M. Frumar, Z. Polak and Z. Cernosek, *J. Non-Cryst. Solids*, 1999, **256 & 257**, 105–110.
28 F. Buciuman, F. Patcas, R. Craciun and D. R. T. Zahn, *Phys. Chem. Chem. Phys.*, 1999, **1**, 185–190.
29 M. C. Bernard, A. H. L. Goff and B. V. Thi, *J. Electrochem. Soc.*, 1993, **140**, 3065–3070.
30 M. Sun, B. Lan, T. Lin, G. Cheng, F. Ye, L. Yu, X. Cheng and X. Zheng, *CrystEngComm*, 2013, **15**, 7010.
31 C. M. Julien, M. Massot and C. Poinsignon, *Spectrochim. Acta, Part A*, 2004, **60**, 689–700.
32 C. Julien, *Solid State Ionics*, 2003, **159**, 345–356.
33 C. Julien and M. Massot, *Phys. Chem. Chem. Phys.*, 2002, **4**, 4226–4235.
34 R. Ma, Y. Bando, L. Zhang and T. Sasaki, *Adv. Mater.*, 2004, **16**, 918–922.
35 P. W. Ruch, D. Cericola, M. Hahn, R. Kötz and A. Wokaun, *J. Electroanal. Chem.*, 2009, **636**, 128–131.
36 L. J. Hardwick, M. Hahn, P. Ruch, M. Holzapfel, W. Scheifele, H. Buqa, F. Krumeich, P. Novák and R. Kötz, *Electrochim. Acta*, 2006, **52**, 675–680.
37 C. H. Liang and C. S. Hwang, *Jpn. J. Appl. Phys.*, 2008, **47**, 1662–1666.
38 M. Chigane and M. Ishikawa, *J. Electroanal. Soc.*, 2000, **147**, 2246–2251.
39 C. C. Hu and T. W. Tsou, *Electrochim. Acta*, 2002, **47**, 3523–3532.
40 M. Richter, A. Trunschke, U. Bentrup, K. W. Brzezinka, E. Schreier, M. Schneider, M. M. Pohl and R. Fricke, *J. Catal.*, 2002, **206**, 98–113.
41 M. Pourbaix, *Atlas of Electrochemical Equilibria in Aqueous Solutions*, National Association of Corrosion Engineers, Houston, TX, 1996.
42 B. Djurfors, J. N. Broughton, M. J. Brett and D. G. Ivey, *Acta Mater.*, 2005, **53**, 957–965.
43 C. H. Wang, S. C. Hsu and J. H. Hu, *J. Power Sources*, 2014, **249**, 1–8.
44 Y. K. Hsu, Y. C. Chen, Y. G. Lin, L. C. Chen and K. H. Chen, *Chem. Commun.*, 2011, **47**, 1252–1254.
45 M. Kalapsazova, R. Stoyanova, E. Zhecheva, G. Tyuliev and D. Nihtianova, *J. Mater. Chem. A*, 2014, **2**, 19383–19395.